J. Fluid Mech. (1993), *vol.* 246, *pp.* 503–527

Turbulent boundary layers subjected to multiple curvatures and pressure gradients

By PROMODE R. BANDYOPADHYAY† AND ANWAR AHMED‡
Mail Stop 170, NASA Langley Research Center Hampton, VA 23665-5225, USA

(Received 30 April 1991 and in revised form 17 June 1992)

The effects of abruptly applied cycles of curvatures and pressure gradients on turbulent boundary layers are examined experimentally. Two two-dimensional curved test surfaces are considered: one has a sequence of concave and convex longitudinal surface curvatures and the other has a sequence of convex and concave curvatures. The choice of the curvature sequences were motivated by a desire to study the asymmetric response of turbulent boundary layers to convex and concave curvatures. The relaxation of a boundary layer from the effects of these two opposite sequences has been compared. The effect of the accompanying sequences of pressure gradient has also been examined but the effect of curvature dominates. The growth of internal layers at the curvature junctions have been studied. Measurements of the Görtler and corner vortex systems have been made. The boundary layer recovering from the sequence of concave to convex curvature has a sustained lower skin friction level than in that recovering from the sequence of convex to concave curvature. The amplification and suppression of turbulence due to the curvature sequences have also been studied.

1. Introduction

The flow over convex and concave surfaces can be expected to be stabilizing and destabilizing, respectively, based on the simple inviscid balance of angular momentum and radial pressure gradient (von Kármán 1934). At the same Reynolds number, decreased and increased radial mixing, compared to that on a flat surface, are therefore indicated in these two types of curvature. However, from this stability consideration alone, it is not clear that, for the same absolute value of the radius of curvature R, the amount of decrease or increase in any mixing-dependent variable like skin friction would be the same if the surface is convex or concave, respectively.

Elsewhere (Bandyopadhyay 1986), an examination of the measurements of turbulent boundary layers over convex and concave surfaces carried out by Ramaprian & Shivaprasad (1977) and Prabhu, Narasimha & Rao (1983) indicated that a turbulent 'boundary layer is slower to respond to a concave curvature than to a convex'. This was termed 'an asymmetric response of the boundary-layer large structures to external forces'. This observation was made simultaneously by Muck, Hoffmann & Bradshaw (1985). Similar behaviour has been observed in positive and negative pressure gradients by Leontev & Fomichev (1983). Such an asymmetric

---

† Present address: Code 8234, Naval Undersea Warfare Center Division, Newport, RI 02841-5047, USA.

‡ On leave from: Aero. Department, Texas A. & M. University.

response is potentially useful in fluids engineering applications: for example, if a boundary layer is subjected to successive regions of equal concave and convex curvatures, it is likely to result in a lower viscous drag compared with that on a flat plate of equal length. The purpose of the present work is to verify this hypothesis.

Since 1986, two computational efforts have also supported this hypothesis. Bandyopadhyay (1989) has computed turbulent boundary layers developing over convex and concave surfaces using the Richardson number formulation of the curvature effect on the equilibrium mixing length l_{eq} (Prandtl 1929; Bradshaw 1969, 1973; So 1975). The effective mixing length l_{eff} is then given by

$$l_{eff} = [1-\alpha(2U/R)/(\partial U/\partial y)]\, l_{eq}, \qquad (1)$$

where α is the Bradshaw constant. In both two-dimensional and axisymmetric bodies, the value of α was 7 in convex surfaces but 3 to 5 in concave surfaces. Asymmetric behaviour was clearly indicated. The origin of the asymmetric response can be seen by casting the Reynolds stress transport equations in a general orthogonal curvilinear coordinate system where the curvature terms appear explicitly (Gatski & Savill 1989; Richmond, Chen & Patel 1986 and Nash & Patel 1972). The equations were derived earlier by So (1975). Gatski & Savill's derivation shows that the asymmetry comes from the nonlinear interactions between the component transport equations. They examined the asymmetry directly by comparing a sequence of concave-to-convex with a sequence of convex-to-concave curvature. Although the modelling did not compute skin friction but only the anisotropy ratio at one point in the outer part of a homogeneous layer, it did demonstrate the asymmetric effect.

When a flat-plate boundary layer encounters a convex surface, its skin friction drops. An attempt is being made to apply this behaviour, called the convex curvature concept of viscous drag reduction (Bandyopadhyay 1990, 1989, 1986; Bushnell 1983), to axisymmetric nose bodies. In the non-separating design, such a nose is characterized by sequences of concave-to-convex-to-flat surfaces applied repeatedly. Computations have shown that such a nose body leads to a lower viscous drag compared to a conventional elliptic nose of equivalent area (although not when compared based on volume). The modelling is fraught with difficulty because the lag behaviour of large eddies in the simultaneous presence of repeatedly applied complex strains of curvature, pressure gradient, lateral divergence and compressibility, is unknown. Therefore, it would be useful to conduct an experiment to verify the aforementioned hypothesis directly in the manner in which the application of the concept of viscous drag reduction is being envisaged, namely, a sequence of concave-to-convex curvature followed by a flat region of recovery from the low skin friction levels.

A low-Reynolds-number incompressible flow experiment in an S-shaped wind tunnel is described. The two identical zero-pressure-gradient turbulent boundary layers developing on the opposite walls are subjected to two different sequences of longitudinal surface curvatures. In one, a concave fetch is followed by a convex fetch whereas in the other, a convex fetch is followed by a concave fetch. The radii (R) and lengths (Δs) of all four curved regions are identical. The two boundary layers are then allowed to relax on flat walls under a zero pressure gradient. Detailed static pressure, mean velocity, skin friction and longitudinal turbulence measurements have been carried out. Particular attention has been paid to the measurement of the three-dimensional nature of curved boundary layers. The asymmetric response has been studied from the points of view of both surface curvature and departure from equilibrium due to pressure gradient.

There have been several experiments on S-shaped ducts (Rehman & Bowyer 1989; Schmidt, Whitelaw & Yianneskis 1987 and others). They simulate the inlets to the air-breathing propulsion engines which are installed at offset locations in aircraft. These ducts are diffusing over their entire length and curvature effects are negligible. Consequently, the turbulent boundary layers in these ducts undergo a very different history of complex strains compared to that in the present study.

2. Details of the experiment

2.1. *Wind tunnel*

A sketch of the wind tunnel constructed for this experiment is shown in figure 1. It is an open circuit tunnel where the air recirculates within the room, which is air conditioned. Air enters the tunnel through a fibreglass contraction cone which contains paper honeycomb and a series of three screens. The contraction entry cross-section is 38.1×38.1 cm^2. The nominal cross-section of the tunnel at the contraction exit is 25.4 cm (span) × 10.2 cm (width). The tunnel has four sets of test sections each 50.4 cm in streamwise length (Δs). The boundary layer is tripped in all four walls at the end of the contraction. The trip wire diameter is 1.6 mm. The turbulent boundary layer is allowed to grow in the first flat length. This is followed by two curved lengths. The nominal radius of curvature R is also 50.4 cm in each curved length, being positive in the convex and negative in the concave walls. The second curved length is followed by another flat length of 50.4 cm where the recovery of the boundary layer from the effects of curvature and pressure gradient can be studied. After this region, there is a diffuser followed by a variable-speed centrifugal fan. Downstream of the contraction, in each of the four test lengths, the widths are enlarged by 5.1 mm to compensate for the boundary-layer growth. This amounted to an expansion of 0.25° normal to each wall.

As figure 1 shows, the curvature sequences were designated as follows: in wall A, a flat length was first followed by a concave, then a convex fetch and finally a flat length; however, in wall B, a flat length was first followed by a convex and then a concave fetch which was followed by a flat length.

Surface pressure taps were located nominally at 5 cm intervals along the centrelines of the two curved sides and also along the span and radial directions at two stations in the curved regions. The station numbers and streamwise (s) coordinates are given in table 1. A reference Pitot tube placed downstream of the contraction at station number 3 was used to monitor the tunnel speed. The experiments were conducted at a reference free-stream speed of 9.0 m/s.

2.2. *Measurements*

The static pressure taps were connected to two scanivalves controlled by a scanner. All pressures were read by 1 Torr head Barocel Transducers and Electronic Manometers whose voltage values were read by HP3456 Digital Voltmeters. Boundary-layer traverses were made using flattened single Pitot tubes of 0.318 mm outer thickness. A programmable traverse gear (Aerotech) controlled by a Personal Computer was used to move the probe. The traverse gear was backlash-free and the programming ability allowed it to be homed to preset near-wall positions for repeated surveys. A cathetometer as well as a calibrated closed-circuit TV system was

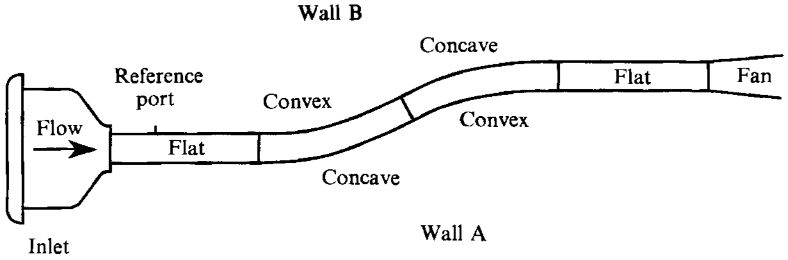

FIGURE 1. Sketch of the S-tunnel. All curved radii = 50.8 cm = length of each flat/curved section.

Station no.	3	4	5	6	7	8	9	11	12	13
s (mm)	127	177.8	228.6	279.4	330.2	381.0	431.8	539.8	590.6	641.4
Surface ←					A, B: Flat			→←		
Station no.	14	15	16	17	18	19	20	21	22	23
s (mm)	692.2	743.0	793.8	844.6	895.4	946.2	997.0	1048	1099	1149.4
Surface				A: Concave/B: Convex				→←		
Station no.	24	25	26	27	28	29	30	31	32	33
s (mm)	1200	1251	1302	1353	1403	1454	1505	1556	1607	1672
Surface					A: Convex/B: Concave			→←		
Station no.	34	35	36	37	38	39	40	41		
s (mm)	1722	1773	1824	1875	1926	1976	2027	2078		
Surface				A, B: Flat					→	

TABLE 1. Measurement stations in walls A and B.

used to determine the origin of surface-normal distances. Traverses were made normal to the surface. The skin friction measurements were made using Preston tubes of diameters (d) 0.71, 1.45 and 2.0 mm.

Consider a curvilinear coordinate system where s, y and z represent distances along the streamwise, surface-normal and spanwise directions, respectively. The origins of s, y and z are respectively at the beginning of the first flat section, at the surface and at the centreline. The symbol s_i is used for internal-layer growth studies and it represents a distance along s but measured from the beginning of a given flat or concave or convex section. The symbol Δs denotes the maximum value of s_i in a given section. The mean velocities are: U along s, U_p the local potential velocity and U_{pw} potential velocity at the wall. The statistics of the fluctuating longitudinal velocity u' are denoted as follows: the symbols u and u^3 stand for $(\overline{u'^2})^{\frac{1}{2}}$ and $\overline{u'^3}$, respectively, where the overbars denote long time averaging. At the curved walls, local mean velocities were calculated from the following expressions (So & Mellor 1972, 1973):

$$U(y)=\left[\frac{2}{\rho}\left\{(P_t-P_{sw})-(P_r-P_{sw})\left(1-\frac{1}{(1+y/R)^2}\right)\right\}\right]^{\frac{1}{2}}, \tag{2}$$

$$U_p=U_{pw}R/(R+y), \tag{3}$$

and

$$P_r-P_{sw}=\tfrac{1}{2}\rho U_{pw}^2, \tag{4}$$

where P_t, P_{sw} and P_r are the total Pitot pressure, local wall static pressure and total Pitot pressure in the potential core, respectively, and ρ is the fluid density.

Because of the presence of pressure gradients, the local coefficient of skin friction was defined in terms of the reference free-stream dynamic head. Thus a comparison in c_f done here is effectively a comparison of the wall shear-stress values (τ_w). The coefficient was defined as follows:

$$c_f = 2U_\tau^2/(\rho U_{\infty\mathrm{ref}}^2), \tag{5}$$

where U_τ is the local friction velocity ($= (\tau_w/\rho)^{\frac{1}{2}}$) and $U_{\infty\mathrm{ref}}$ is the reference incoming free-stream velocity (9.0 m/s) measured at $s = 127$ mm (station 3) in the first flat section. The superscript + denotes non-dimensionalization by the wall-layer velocity scale U_τ and the lengthscale ν/U_τ, i.e. U^+, y^+ and u^+.

Hot-wire measurements were made using a DISA 55P11 single platinum-coated tungsten wire probe 1 mm in length and 5 μm in diameter. The wire was run by a TSI constant-temperature anemometer and a linearizer. The wire was calibrated in the free stream near the contraction exit. The wire output was digitized and analysed using a programmable Analogic Data 6000 analyser. Time records of hot-wire signals consisted of 1.65×10^4 data points sampled at 20 kHz. All control and measurement instruments were placed on the GPIB bus of a Personal Computer which was used for data acquisition. The data analysis was carried out on other computers.

3. Surface pressure distributions

The local coefficient of pressure c_p was defined as

$$c_p = (p - p_3)/q_3, \tag{6}$$

where p is the local wall static pressure, p_3 is p at station 3 and q_3 is free-stream dynamic head ($= \frac{1}{2}\rho U_{\infty\mathrm{ref}}^2$) at reference station 3.

3.1. *Streamwise*

The streamwise wall static pressure distribution is shown in figure 2(*a*). The spline-fit pressure gradient is shown in figure 2(*b*). In both walls, there are regions of zero pressure gradient in the two flat sections, namely where the flow initially develops and finally recovers, and also in a segment in each curved length.

The figures show that, except in the regions of 'sustained' zero values of c_p, the pressure and its first (and second) derivatives are not the mirror images of each other either in absolute values or in the location of their maxima and minima.

3.2. *Radial and spanwise*

The radial and spanwise surface pressure distributions were measured at two streamwise stations, namely after the onset of the first curvature and at the end of the second curvature. The curved wall span was positioned vertically for ease of traverse. The flat sidewalls lying in the radial direction were, therefore, the tunnel top and bottom walls. The static pressure taps were located along the upward span starting from the two opposite curved wall centrelines which met radially in the tunnel top wall. The measurements are shown in figure 3.

Figure 3(*a*) shows that the spanwise pressure distributions at both convex walls are smooth and similar. However, the concave distributions are dissimilar; they are non-uniform near the corners and larger perturbations are present at wall B than at wall A. Spanwise skin-friction measurements presented in §6 show that at wall B at $s = 1480$ mm, the corner flows extend over most of the span. From a potential flow consideration, radially outward, the static pressure should increase linearly since the

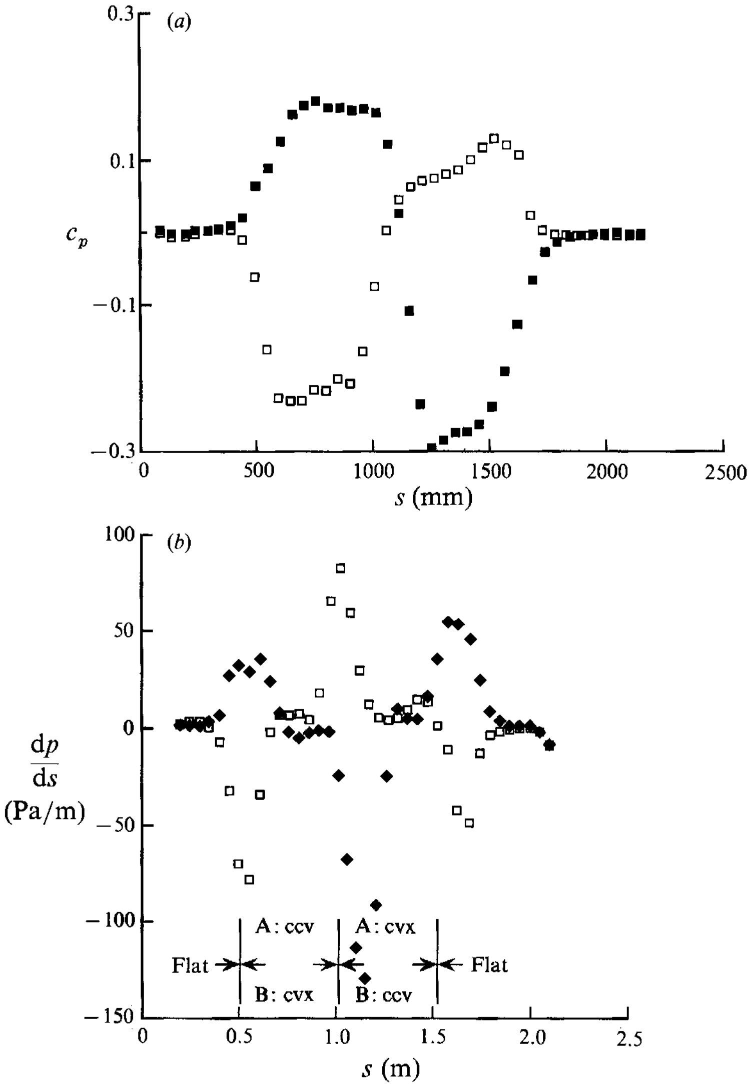

FIGURE 2. Longitudinal distributions of (*a*) mid-plane surface pressure and (*b*) pressure gradient. Solid symbols, wall A; open symbols, wall B.

boundary-layer thickness is small compared to the radius of curvature and figure 3 (*b*) shows that it does so approximately. Particularly at $s = 1480$ mm, the radial distribution adjacent to the concave wall shows an early deviation from linearity unlike that near the corner with the convex wall. The longitudinal, spanwise and radial surface pressure distributions, therefore, show that the pressure histories at the two curved walls are different.

4. Longitudinal development of the boundary layer

4.1. *Skin friction*

The local values of c_f were determined from the mean velocity profiles and Preston tube measurements. In the curved regions, frequently there were few data points in the measured velocity profile which were in the log layer. A modified Clauser method

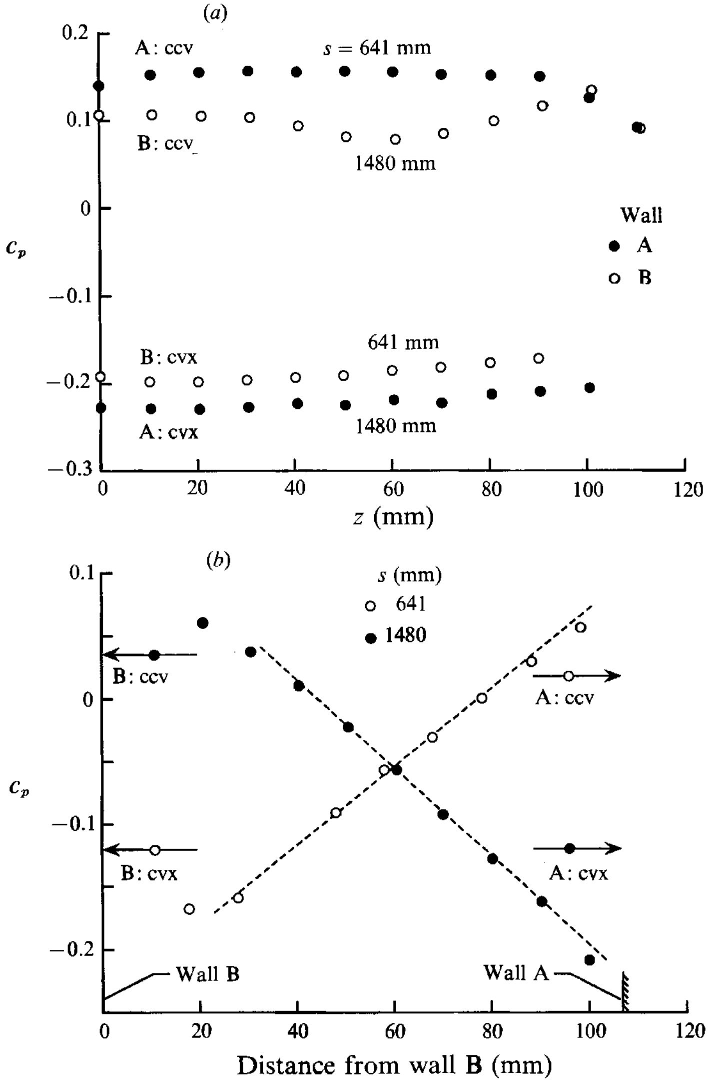

FIGURE 3. Distributions of (*a*) spanwise and (*b*) radial surface pressure in the first and second curved sections.

was therefore used to determine c_f from the measured velocity profiles (Bandyopadhyay 1988). A flat-plate zero-pressure-gradient velocity profile in wall-layer variables is universal in the viscous sublayer, buffer layer and log layer. For various perturbations considered below, the log layer may not exist. Therefore, the measured velocity profiles were closely fitted to an analytical form of this universal distribution to obtain the friction velocity U_τ from which c_f was computed. However, the fit was sought for $y \rightarrow 0$ and not in the log layer. Several representative velocity profiles from each test section in the fitted wall-layer-variable form are shown in figure 4. Within the first flat regions, the entire inner layer displays the universal form.

It is known that log-layer behaviour changes differently at separation and relaminarization. In the former, the width of the log region decreases gradually while in the latter the profile departs from the log law abruptly. Hot-wire measurements have not indicated any relaminarization and tuft tests also indicated the absence of

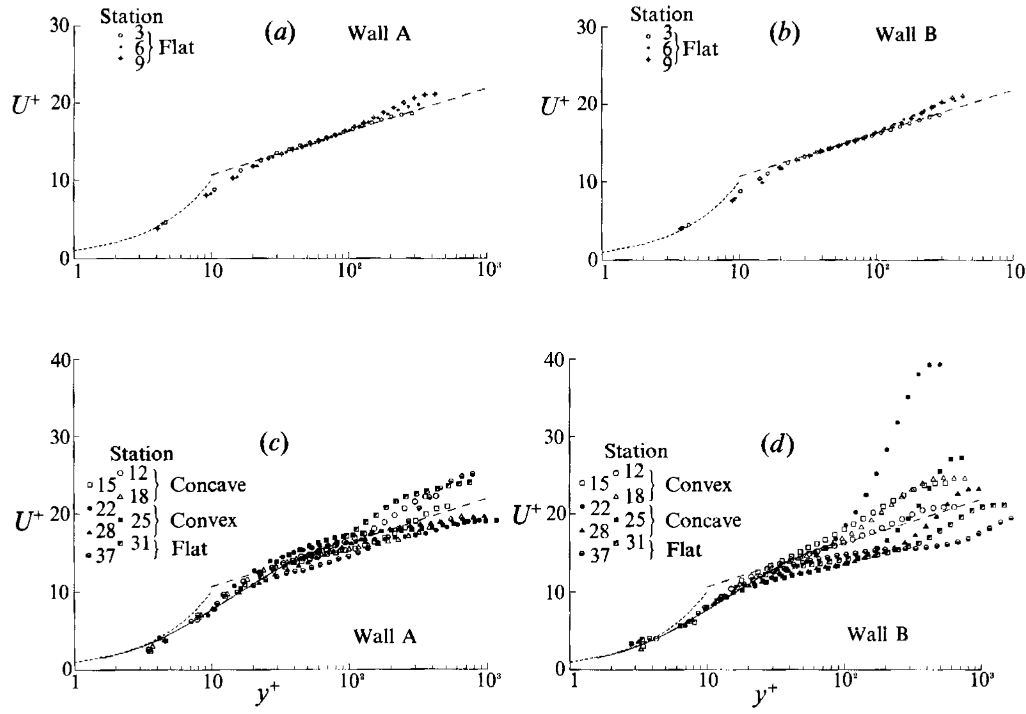

FIGURE 4. Mean velocity profiles in wall-layer variables: ——, $U^+ = 5.62 \log y^+ + 5.0$; ----, $U^+ = y^+$.

any separation. The maximum and minimum values of the pressure gradient parameter, Δ ($= (\nu/\rho U_\tau^3)(\mathrm{d}p/\mathrm{d}s)$) are 0.083 and -0.015, respectively. Separation and onset of the relaminarization process can be expected when $\Delta > 0.09$ and $\leqslant -0.018$, respectively (Patel 1965). The present values are within these limits.

The log law occupies a central position in the description of a turbulent boundary layer. The effects of low Reynolds number, curvature and the existence of unusually large scales in the outer layer on the log law in the present flow need to be discussed. (The effects of pressure gradient on the log law have already been considered.) In zero-pressure-gradient flat-plate boundary layers, the lowest Reynolds number at which a log layer has been reported to exist are as follows. A regular (see figure 4) distinct log law with a universal wall layer has been reported in the experiments carried out at $Re_\theta = 500$ by Purtell, Klebanoff & Buckley (1981), at $Re_\theta = 617$ by Erm, Smits & Joubert (1985) and at $Re_\theta = 354$ by Smits, Matheson & Joubert (1983). In the numerical simulation works of Tsai & Leslie (1990), a log law appears at $Re_\theta = 505$, and at 670 in those of Spalart (1988). It is believed that a regular log law first appears at $300 < Re_\theta < 500$. In the present work, $Re_\theta > 500$ downstream of port 3. Therefore, in the flat regions before the curved fetches, the boundary layer is expected to grow to one with a regular and distinct log law. Figure 4 shows that it does so.

Since the present Re_θ values are high enough, the departures from the log law in the present data are not due to low-Reynolds-number effects. In the curved channel simulation work of Moser & Moin (1987), at about the same Reynolds number, the velocity profile remains below the log law over the concave surface and it moves above the log law over the convex surface. Therefore, in the present data, the

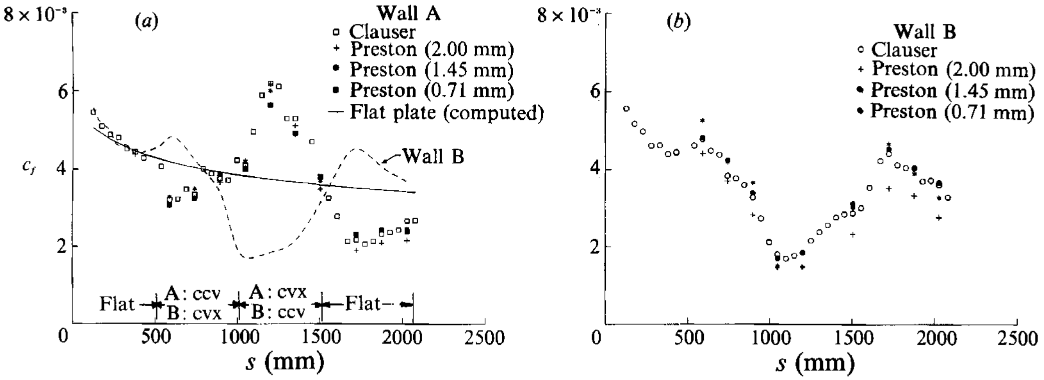

FIGURE 5. Longitudinal centreline skin friction distributions.

departures above and below the log law in the convex and concave regions, respectively, are due to curvature. Finally, the velocity profile is known to depart from the log law even on a flat surface when the outer layer contains large scales (Smits, Young & Bradshaw 1979). These large scales appear over and after a concave fetch (Moser & Moin 1987) and after a flow reattachment as in a backward-facing step. In the present data, in the final flat region, particularly at wall B, the departure from the log law can be ascribed to the large-scale longitudinal vortices in the corners and those formed by the upstream concave curvatures. In corroborating evidence to be presented in §8, these regions, where the mean velocity dips below the log law, are characterized by an amplification of the u-turbulence intensity indicating the presence of a large-scale mixing mechanism. The present departures from the log law are therefore primarily representative of curvature effects.

The longitudinal distributions of the centreline skin friction are shown in figure 5. The modified Clauser and all Preston tube measurements compare well except in the later part of the flat recovery section on wall B where the 2.0 mm diameter Preston tube data are inaccurate because the $U_\tau d/\nu$ value of 50 is larger than 30, the local thickness of the universal region.

If the effect of pressure gradient is ignored, at wall A the wall shear stress should drop in the initial flat section up to $s = 500$ mm because of increasing Re_θ, should increase for $500 < s < 1000$ mm because of concave curvature, should drop for $1000 < s < 1500$ mm due to convex curvature and then increase to the local flat-plate equilibrium level in the flat region $s > 1500$ mm. On the other hand, based on pressure gradient alone (figure 2*b*), the wall shear stress should drop for $0 < s < 900$ mm ($\mathrm{d}p/\mathrm{d}s \geqslant 0$), increase for $900 < s < 1300$ ($\mathrm{d}p/\mathrm{d}s < 0$) and decrease thereafter. In the measurements, wall shear stress drops for $s < 600$ mm, increases for $600 < s < 1200$ mm, drops for $1200 < s < 1750$ mm and rises thereafter. So, in the two curved regions, curvature effects dominate pressure gradient effects.

The secondary effect of the pressure gradient is as follows. The drop in τ_w in $500 < s < 600$ mm in spite of concave curvature is attributable to $\mathrm{d}p/\mathrm{d}s > 0$ or to an inherent slow response in the onset of concave curvature or due to both. This lag length is about $62.5\theta_f = 4\delta_f$, where the subscript f denotes the value of the variables (equation (8)) at the end of the flat length. In the region $900 < s < 1000$ mm, both $\mathrm{d}p/\mathrm{d}s$ and curvature indicate an increase in τ_w and it does so. Owing to the presence of a spanwise Görtler roll structure, a concave turbulent boundary layer can be considered to have a longer memory compared to that for $\mathrm{d}p/\mathrm{d}s \geqslant 0$ or for flat and convex curvatures. Now, a convex curvature is known to lower τ_w immediately (So

& Mellor 1972, 1973) when preceded by a flat-plate boundary layer with $\mathrm{d}p/\mathrm{d}s = 0$ and it is likely to behave similarly when $\mathrm{d}p/\mathrm{d}s < 0$ also. Therefore, for $1000 < s < 1200$ mm, the increase in τ_w in spite of the onset of convex curvature is attributable both to the memory effect of the Görtler roll cells of the previous concave region and to $\mathrm{d}p/\mathrm{d}s < 0$. This lag length is about $80\theta_c = 6.6\delta_c$ where the subscript c denotes the value at the end of the concave region. However, the continued drop in τ_w after the removal of convex curvature for $1500 < s < 1750$ mm seems due to $\mathrm{d}p/\mathrm{d}s > 0$ alone.

The skin friction distribution along wall B can also be analysed similarly. Considering curvature effects alone, τ_w should drop at a slow rate in the flat region $0 < s < 500$ mm increasing to a faster rate in the convex region $500 < s < 1000$ mm, should increase in the concave region $1000 < s < 1500$ mm and then drop at a slow rate for $s > 1500$ mm. Based on pressure gradient alone (figure 2*b*), τ_w should drop slowly for $0 < s < 300$ mm because $\mathrm{d}p/\mathrm{d}s = 0$, should increase for $300 < s < 700$ mm because $\mathrm{d}p/\mathrm{d}s < 0$, should decrease for $700 < s < 1500$ mm because $\mathrm{d}p/\mathrm{d}s \geqslant 0$, increase for $1500 < s < 1800$ mm because $\mathrm{d}p/\mathrm{d}s < 0$ and then for $s > 1800$ mm, should decrease slowly at a rate characteristic of a flat-plate zero pressure gradient. On the other hand, the measurements show that τ_w drops for $0 < s < 1200$ mm at three rates: at an initial rate for $0 < s < 300$ mm which slows down for $300 < s < 600$ mm and then drops at the highest rate for $600 < s < 1200$ mm. In the range $1200 < s < 1750$ mm, τ_w increases rapidly and then drops for $s > 1750$ mm. Therefore, in the curved regions, the skin friction behaviour is, primarily, curvature dominated.

The secondary effect of the pressure gradient is as follows. The virtual arrest of the τ_w drop in the flat region $300 < s < 500$ mm and in the initial convex region $500 < s < 600$ mm is due to $\mathrm{d}p/\mathrm{d}s < 0$. In the initial concave region, $1000 < s < 1200$ mm, the continued drop in skin friction is attributable both to $\mathrm{d}p/\mathrm{d}s > 0$ and to the higher time constant for the onset of concave curvature effects. In the flat-wall range $1500 < s < 1750$ mm, τ_w continues to rise not only due to $\mathrm{d}p/\mathrm{d}s < 0$ but also quite probably due to the long lifetimes of the pre-existing longitudinal large-scale vortices.

In figure 5(*a*), the streamwise skin friction distributions at both walls are compared with the flat-plate zero-pressure-gradient distribution. The latter was calculated using the Schultz–Grunow relationship, namely $c_f = 0.37[\log(Re_s)]^{-2.584}$, where $Re_s = [U_e(s + 17.98\ \mathrm{cm})/\nu]$ (Schlichting 1979, p. 643). The virtual origin, located 17.98 cm upstream of $s = 0$, was estimated by matching the measured skin friction at $s = 33.02$ cm. This also agrees with figure 6. In the final flat region, the wall A distribution lies below the flat-plate values and the relaxation is incomplete.

The nett pressure and viscous friction drags have been calculated using the centreline local pressure and skin friction distributions, shown in figures 2(*a*) and 5 respectively, and the spanwise skin friction distributions shown later in figure 9. The two-dimensional pressure drag coefficient is defined as $C_{dp} = [\int_0^Y p(s)\,\mathrm{d}\xi]/(q_3 L_c)$, where ξ is the projected distance in the vertical direction, Y is the overall vertical offset due to a curved fetch and L_c is the reference curved length of 50.8 cm. The values of C_{dp} are: wall A (concave: 1.12×10^{-3} and convex: 0.93×10^{-3}) and wall B (convex: 0.95×10^{-3} and concave: 1.08×10^{-3}). Thus, the total pressure drag is nearly the same (within 1%) in both walls. The three-dimensional friction drag is defined as $C_{df} = [\int \tau_w(s, z)\,\mathrm{d}A_x]/[q_3(L\ 190\ \mathrm{mm})]$ where A_x is the projected surface area in the axial direction, being integrated over the span $-95 \leqslant z \leqslant 95$ mm, and L is the reference length of 152.4 cm, which is the sum of the two curved lengths and the final flat length of recovery. Assuming a two-dimensional flow, the value of C_{df} at the flat wall is 0.0038. Taking the three-dimensional flow into account, the values of C_{df} are

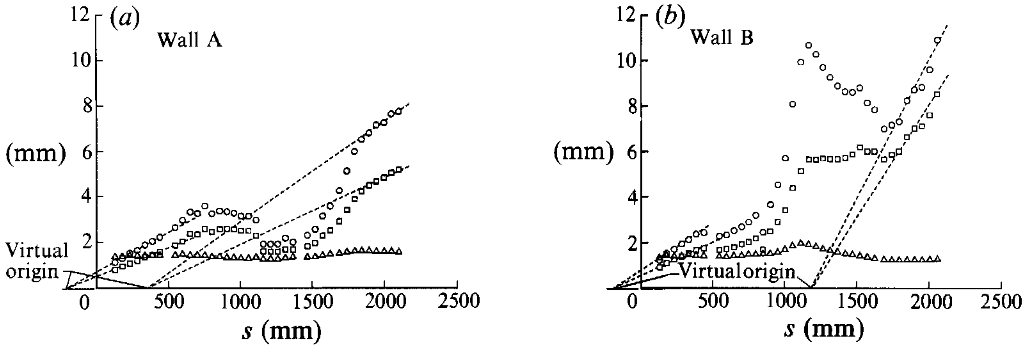

FIGURE 6. Overall distributions of the centreline boundary-layer integral quantities: ○, δ^*; □, θ; △, H.

0.0028 at wall A and 0.0032 at wall B. Thus, the wall A friction drag is 12% below the wall B friction drag. Since the relaxation in the final flat region is far from complete, given a longer relaxation length, the friction drag in wall A will be comparatively even lower. Also note that in the present work, the geometries of the concave and convex fetches are identical because the purpose is to document the asymmetric response. However, in an actual drag reduction application, the concave fetches would be far less than the convex fetches.

4.2. *Integral quantities*

Mean velocity profiles were measured on both walls A and B along the centreline and the boundary-layer integral quantities, viz. displacement thickness (δ^*), momentum thickness (θ), shape factor (H) and Reynolds number Re_θ were calculated from those. These quantities were defined as follows:

$$\delta^* = \int_0^\delta (1-U/U_e)\,\mathrm{d}y, \tag{7}$$

$$\theta = \int_0^\delta U/U_e(1-U/U_e)\,\mathrm{d}y, \tag{8}$$

$$H = \delta^*/\theta, \tag{9}$$

$$Re_\theta = U_e\theta/\nu, \tag{10}$$

where U_e is the edge velocity obtained from (2) and ν is the kinematic viscosity of the fluid. The subscript 0 denotes values at $s_i = 0$ and δ denotes the value of y where $U = 0.995U_e$.

The overall distributions of these quantities at walls A and B are shown in figure 6. At both walls, in those parts of the two flat regions where $\mathrm{d}p/\mathrm{d}s \approx 0$, H is nearly constant. This implies a relaxation toward equilibrium. At both walls, the early concave and convex regions have an adverse and a favourable pressure gradient, respectively. At wall B, the lengthscales increase much more rapidly in the adverse-pressure-gradient region where the maximum amplitude is higher than that at wall A.

4.3. *Defect profiles*

The defect profiles are shown in figure 7 where each flat or curved section is grouped separately. In the first flat sections, although the profiles appear to have collapsed, a closer scrutiny reveals that there is a very weak but systematic variation with s.

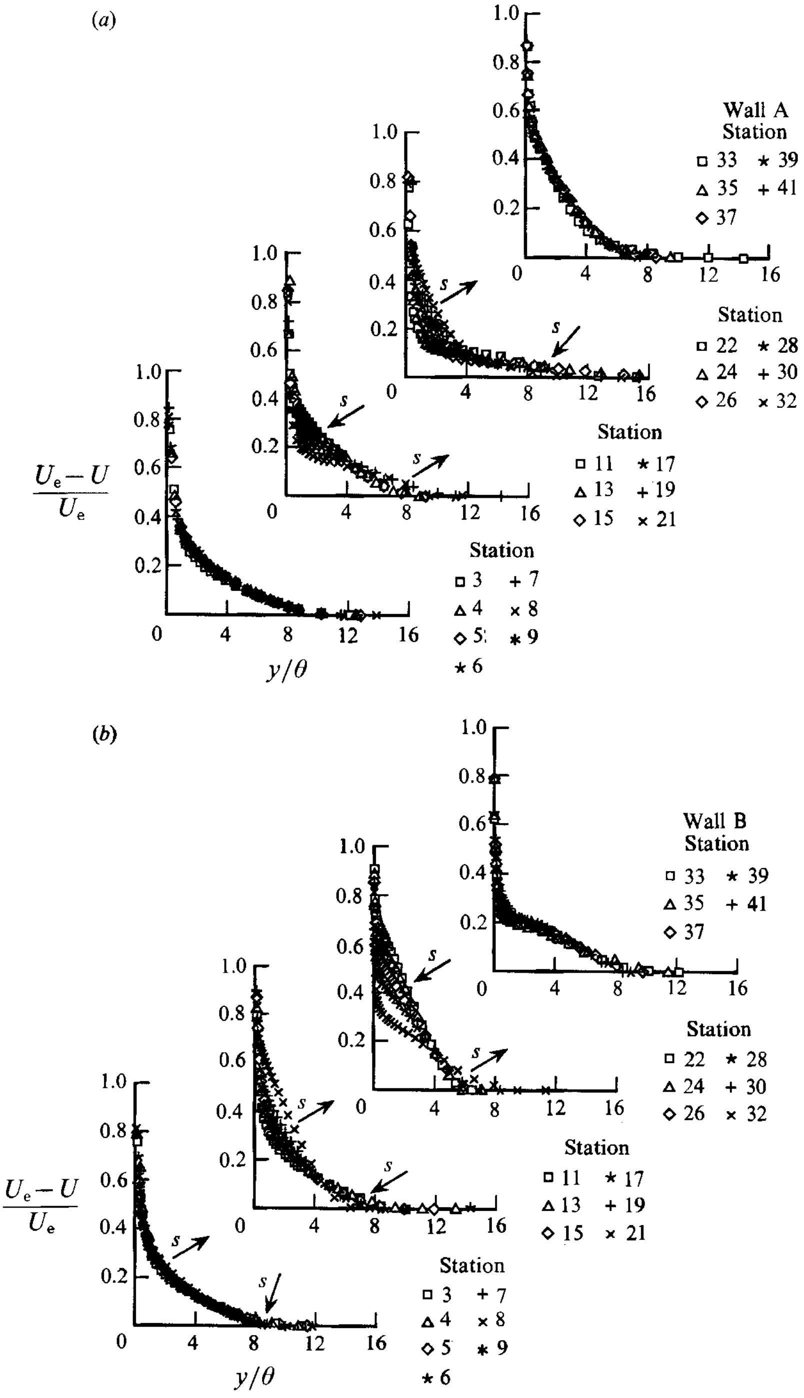

FIGURE 7. Velocity defect profiles.

With few exceptions, in the curved regions the profiles cross at a characteristic value of y/θ. This height, namely y_c/θ, is 4.2 to 4.5 in the curved regions. An observer at $y = y_c$ while convecting downstream at cU_e where c is 0.87 to 0.93, will find the following. If the surface is concave, at a given y/θ, where $y/\theta < y_c/\theta$, the fluid accelerates downstream, whereas at an y/θ where $y/\theta > y_c/\theta$, the fluid decelerates. The trend is opposite in the convex fetch: with increasing s, the fluid decelerates where $y/\theta < y_c/\theta$ but accelerates where $y/\theta > y_c/\theta$. Figures 4 and 18 similarly show that the strength of the wake component, which is a measure of the energy of the outer large eddy, increases in the convex and decreases in the concave fetch. The curvature-based demarcation of the accelerating and decelerating layers at a constant y/θ is intriguing.

5. Effects of pressure gradient

The Clauser parameter G for a velocity profile can be defined as

$$G = \int_0^\delta [(U_e - U)/U_\tau]^2 \, dy \Big/ \int_0^\delta [(U_e - U)/U_\tau] \, dy. \tag{11}$$

The characteristic value of G is 6 to 7 in a zero-pressure-gradient equilibrium turbulent boundary layer. The departure and return to equilibrium can be described in a (G, β)-plane where β is the ratio of pressure to friction forces given by

$$\beta = (\delta^*/\tau_w)(dp/ds). \tag{12}$$

The (G, β) trajectories in figure 8 show three features. (i) The value of G reached is 6 in the first flat fetch but, it is far from equilibrium in the final flat section, particularly at wall A. A much longer recovery section was clearly required. (ii) The flat junctions are within $0 < \beta < 1$ at wall A and within $-1 < \beta < 0$ at wall B. In wall A, the concave-to-convex junction is located near the minimum value of β, whereas in wall B the convex-to-concave junction is located near the maximum value of β. (iii) In the largest loops (A: 7–8–9; B: 3–4–5–6), the departure from equilibrium (outgoing trajectories A(7–8) and B(3–4)) is linear, but the return (incoming trajectories A(8–9) and B(4–5–6)) is nonlinear. This can be termed an hysteresis of the large eddies. The linear nature of the departure from equilibrium has also been observed in a weakly adverse-pressure-gradient flat-plate boundary layer relaxing from the perturbation due to a drag-reducing outer-layer device (Bandyopadhyay 1986). A similar but weaker hysteresis is present in the $-\beta$ loop as well. The importance of the sign of $d\beta/ds$ to the large-eddy response was recognized by Nash (1965). To model relaminarizing and separating turbulent boundary layers accurately, in addition to β, the effect of $d\beta/ds$ should also be considered.

6. Three-dimensional nature of the curved boundary layers

The spanwise distributions of the local skin friction coefficient defined with respect to the reference dynamic head at station 3, are shown in figure 9. These measurements have been carried out with Preston tubes of diameter 0.71 mm. These measurements have been analysed (i) to determine if the non-uniformities are Görtler-like and (ii) to compare the growth characteristics of the corner vortices at the two walls.

6.1. *Görtler vortex*

The laminar Görtler number Go can be defined as

$$Go = (U_e \theta/\nu)(\theta/R)^{\frac{1}{2}}. \tag{13}$$

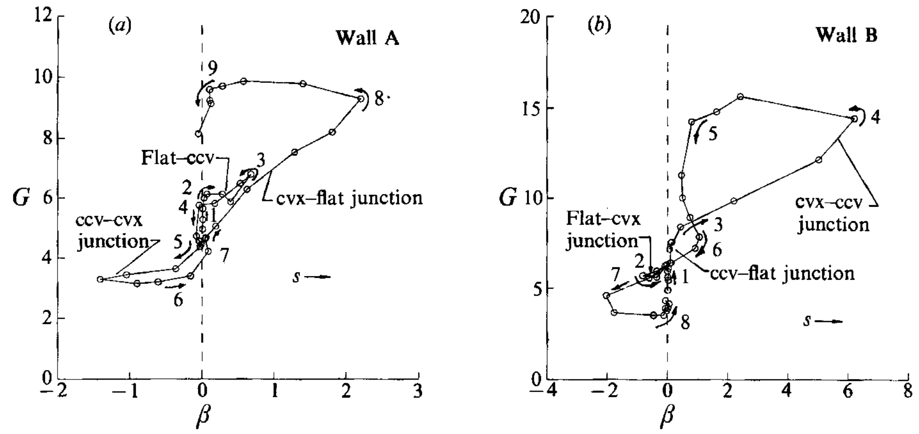

FIGURE 8. Pressure gradient trajectories of the departure from and return to equilibrium of the mean flow.

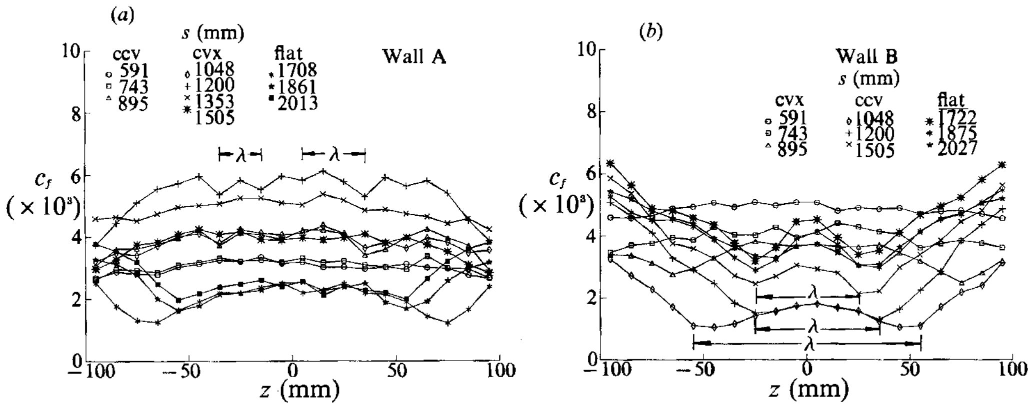

FIGURE 9. Spanwise distributions of skin friction.

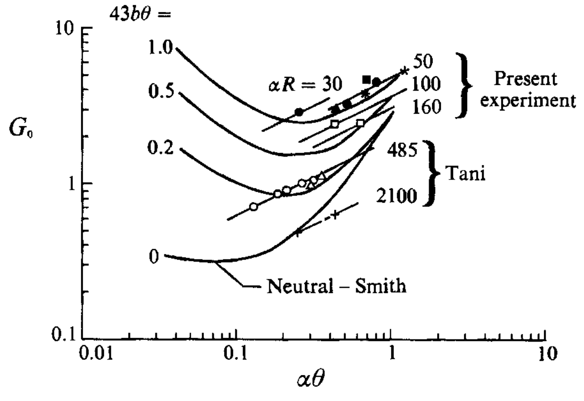

FIGURE 10. Comparison of spanwise wavenumbers in the concave walls with other measurements in zero-pressure-gradient turbulent boundary layers. So & Mellor (1975): $R = 0.4$ to 0.6 m; $U_e =$ 20 m/s; $\alpha R = 67$ (▲, □) and 84 (*). Tani 1962): R, $U_e = 5$ m, 7 m/s (△), 5 m, 20 m/s (○), 10 m, 11 m/s (+).

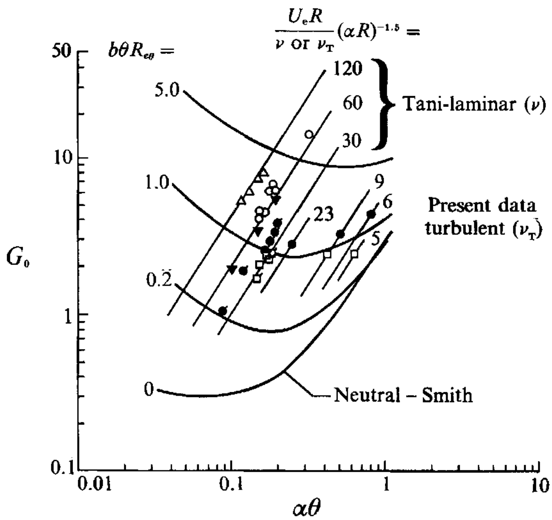

FIGURE 11. Comparison of spanwise wavenumbers in the concave walls with Tani's measurements in laminar boundary layers.

Similarly, the turbulent Görtler number can be defined by replacing ν by ν_T, where ν_T is the turbulent eddy viscosity. The value of ν_T can be calculated from Clauser's (1956) relationship: $\nu_T = 0.018 U_e \delta^*$. If λ (cm) is the wavelength of the spanwise non-uniformities in c_f, the wavenumber α in 2π (cm) is then given by $2\pi/\lambda$. The amplification rate is given by b.

The spanwise non-uniformities in the concave surfaces marked on figure 9 are compared in figure 10 with Tani's (1962) and So & Mellor's (1975) measurements on concave surfaces in zero-pressure-gradient turbulent boundary layers. The measurements are also compared with Smith's (1955) theory. The present measurements are in the unstable region and the trend in αR agrees with others.

The present turbulent measurements are compared with Tani's (1962) laminar measurements in figure 11. The trend in $[U_e R/(\nu \text{ or } \nu_T)][\alpha R]^{-1.5}$ is correct.

6.2. *Corner vortex*

If c_f increases as a corner is approached while traversing along span, a (positive) corner vortex is assumed to exist. (Negative corner vortices, defined similarly, are mostly weaker and have not been studied.) To define the sizes of the corner convex, Δz_l and Δz_r denote spanwise distances from the left and right corners (figure 9), respectively, to the location of the first trough in the c_f-distribution. The strength is defined as the difference between the c_f values at $z = \pm 95$ mm and that at Δz_l and Δz_r, as the case may be. The streamwise growth of the size and strength of the corner vortices are shown in figure 12. Convex curvature can allow some amplification, but eventually it suppresses positive corner vortices and replaces them with negative vortices (figure 9*a*). However, positive corner vortices appear in the flat regions and primarily in the concave region of wall B. At both walls, the strength increases where dp/ds is positive (cf. figure 2*b*). Initially, the strength increases with the size. At wall B, the drop in the strength while the *size stabilizes* is attributable to $-dp/ds$. The size and strength of the corner vortices in the concave and flat regions are determined by dp/ds.

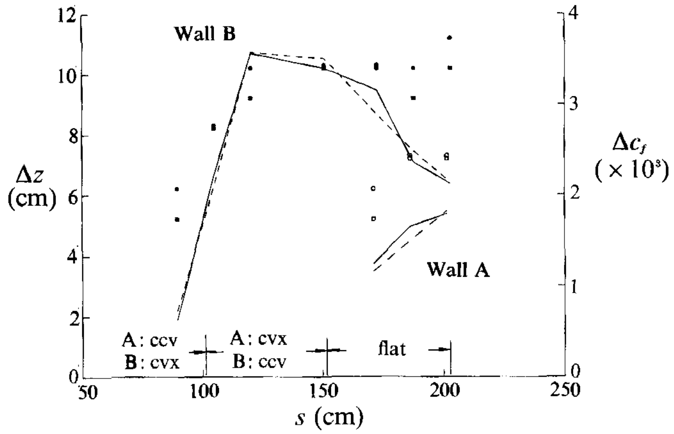

FIGURE 12. Growth of the corner boundary layers. Subscripts l and r denote $-z$ and z, respectively. ●, ○, Δz_l; □, ■, Δz_r; ——, Δc_{fl}; – – –, Δc_{fr}.

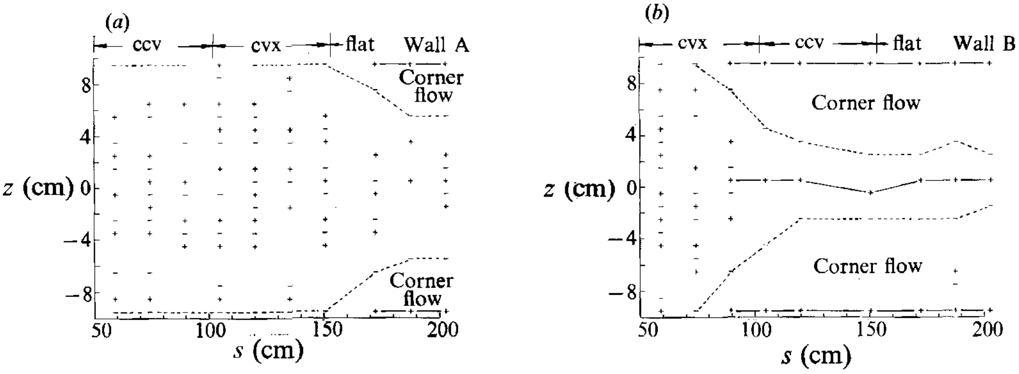

FIGURE 13. Phase plot of the spanwise non-uniformities. Symbols: +, crest in c_f; −, trough.

6.3. *Phase plot of the spanwise non-uniformities*

Figure 13 shows phase plots of the longitudinal vortex systems. The (s, z) locations of the crests and troughs in the c_f-distributions are marked by the symbols + and −, respectively. The crests and troughs were determined from the change in sign of $\mathrm{d}c_f/\mathrm{d}z$ which was calculated linearly using neighbouring measurements.

Figure 13 shows two features. (i) The corner vortex extends over a greater region on wall B. The presence of the convex region between the concave and the final flat lengths on wall A causes a weaker corner vortex system. (ii) The origins of the regions marked corner flows are also the locations of a phase reversal.

At wall B, there are two sources of three-dimensionality, namely the corner flow and the Görtler vortices in the mid-region of the curved wall originating in the concave fetch. Although the corner vortex covers a large extent of the span, after a rapid initial growth its size stabilizes (figures 12 and 13). Its spanwise encroachment stops at about $s = 1200$ mm, where the Görtler vortices also stabilize (figure 9*b*). The following summary of results (i–vi) show that the curvature effects are just as clear in the mid-region of wall B. (i) The asymptotic convex curvature effect is reached at both walls (see collapse of walls A and B with the zero-pressure-gradient asymptote in figure 18*a*, to be introduced later). (ii) In figure 6, the integral lengths grow linearly with a common virtual origin in the final flat regions. (iii) In figure 8, the value of G at wall B has nearly returned to the zero-pressure-gradient flat-plate level. (iv) Figure 17(*b*), introduced later, shows that a new internal layer has formed at the concave–final flat region junction as expected in spite of the corner flow. (v) Figure 5(*a*) shows that, in the final flat region, the rate of relaxation of c_f to the two-dimensional flat-plate level at walls A and B are similar. As a consistency check, walls A and B data cross over the flat-plate line at roughly the same streamwise locations. (vi) Finally, the Görtler wave lengths of wall B follow the right trend in spite of the corner vortex flows (figures 10 and 11). The conclusion therefore is that, for wall B, the corner flow and the mid-region Görtler flow are autonomous and have reached an equilibrium level of coexistence.

7. Internal layers

Table 2 is a summary of the outer- and inner-layer curvature parameters at the curvature junctions. When a convex curvature perturbation is suddenly applied to a flat surface, an internal layer grows when $\Delta R\nu/U_\tau > 0.373\times10^{-4}$ where $\Delta R = (1/R_2 - 1/R_1)$, R_1 and R_2 being the radii of curvature on two sides of the curvature junction (Baskaran, Smits & Joubert 1987). Computations show that, in curved flows, internal layers are more difficult to recognize in velocity profiles (U versus y) than in Reynolds stress and turbulent kinetic energy (Kim 1989).

Before Baskaran *et al.*'s work, the effect of convex curvature was commonly described by the outer layer parameter δ/R. An asymptotic curvature effect is produced when $\delta_0/R > 0.05$ (Gillis & Johnston 1983; Bandyopadhyay 1986). Bandyopadhyay (1990) has shown that the above-mentioned outer- and inner-layer parameter limits for the strong curvature effect are reached simultaneously.

Since timescales are small near a wall, it can be expected to respond to a wall perturbation before the outer layer. An internal layer can be expected to grow near a wall starting at a large local curvature discontinuity. The velocity profile in such a layer will depend on (τ_w, y, α) where $\alpha = \partial\tau/\partial y$. Dimensional considerations show that $\partial U/\partial y \sim (\alpha/y)^{\frac{1}{2}}$. If α is a constant within the layer, integration yields $U \sim y^{\frac{1}{2}}$ (Antonia & Luxton 1971; Townsend 1976, p. 302).

Figure 14 shows the velocity profiles in $(U, y)^{\frac{1}{2}}$ coordinates in the four curved regions. In all of them, as $y \rightarrow 0$, $\mathrm{d}U/\mathrm{d}y^{\frac{1}{2}} \rightarrow$ constant values. In the two convex regions, there is an additional layer where $\mathrm{d}U/\mathrm{d}y^{\frac{1}{2}}$ is constant whose thickness also grows downstream.

7.1. *Skin friction from internal-layer considerations*

The fact that α is a constant within the near-wall internal layer can also be verified from the measurements of $-\overline{uv}$ given in figure 12 of Antonia & Luxton (1971). These data further show that these constant values of $\mathrm{d}(-\overline{uv})/\mathrm{d}y$ within the internal layers vary with s in the same manner as τ_w does. In other words, $\frac{1}{4}(\mathrm{d}U/\mathrm{d}y^{\frac{1}{2}})^2 \propto \tau_w$ where $\tau \rightarrow \tau_w$ as $y \rightarrow 0$ and the constant of proportionality has the dimension of length. Assuming that the same value of the length constant applies at all stations on both walls, its value was obtained by calibrating the internal-layer slope data against the local c_f value at one station. The friction coefficient calculated from the internal-layer slope data is then given by $c_{fi} = \frac{1}{4}\rho[(\mathrm{d}U/\mathrm{d}y^{\frac{1}{2}})^2]\,C/q_3$, where $C = 0.0125$ mm. Figure 15 shows that the values of c_{fi} compare qualitatively with the c_f versus s data. Since c_{fi} is derived from the square of the slope, some scatter is to be expected. The physical significance of the length constant is not clear. Interestingly, the estimates of skin friction could be obtained without any recourse to the log layer and in a flow where

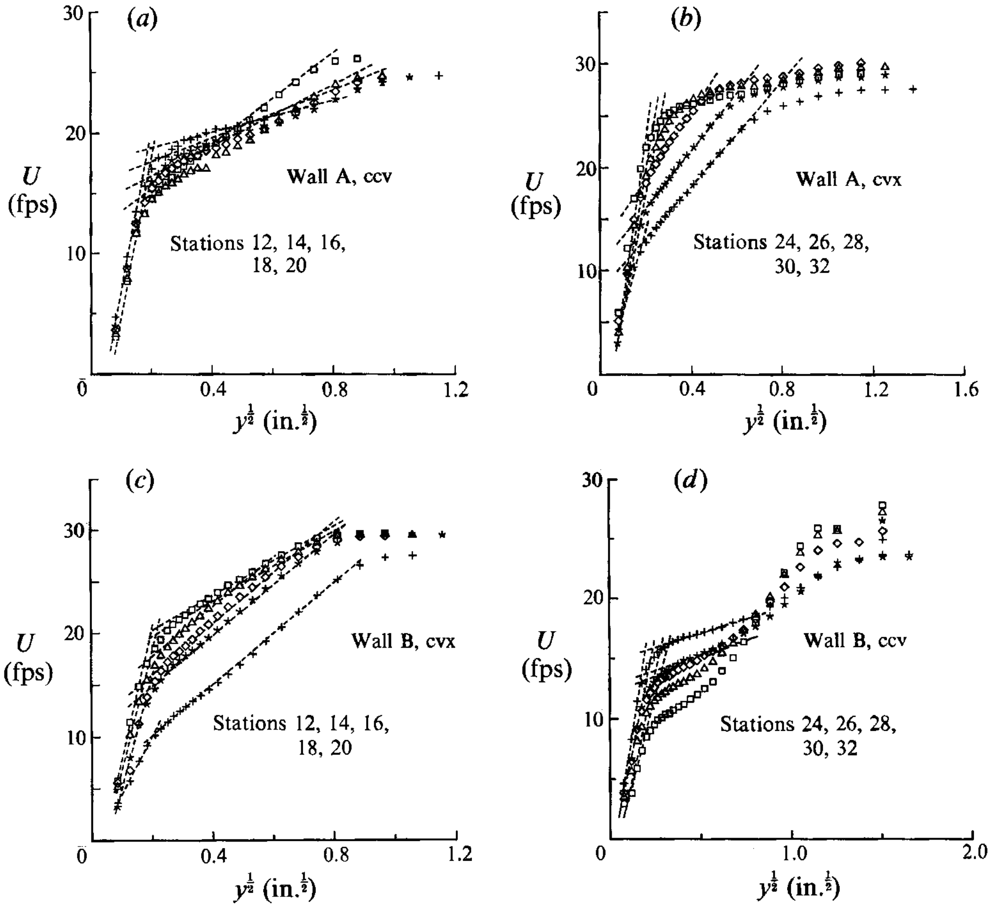

FIGURE 14. Curved wall mean velocity profiles in internal-layer coordinates. □, stations 12 and 24; △, 14 and 26; ◇, 16 and 28; ✱, 18 and 30; +, 20 and 32.

Junction	Flat-to-concave	Flat-to-convex	Concave-to-convex	Convex-to-concave	Convex-to-flat	Concave-to-flat
	Wall A	Wall B	Wall A	Wall B	Wall A	Wall B
δ_0/R	0.0385	0.0385	0.0657	0.055	0.0657	0.135
$\Delta R\nu/U_\tau \times 10^4$	0.7328	0.7284	1.508	1.8554	0.949	0.844

TABLE 2. Curvature parameters at curvature junctions.

the external condition is changing suddenly and repeatedly. The main point however is that this shows *directly* that thin near-wall internal layers form at each curvature junction.

7.2. *Effects of curvature on outer-layer lengthscales*

The outer-layer profiles of $\mathrm{d}U/\mathrm{d}y^{\frac{1}{2}}$ in the curved lengths are shown in figure 16. On wall A, the effect of the convex curvature is to shrink the thickness of the layer where the slope is constant. In the convex section of wall B, the constant-α layer hardly moves. In contrast, in the concave regions of both walls, the location of peak or constant α grows with s.

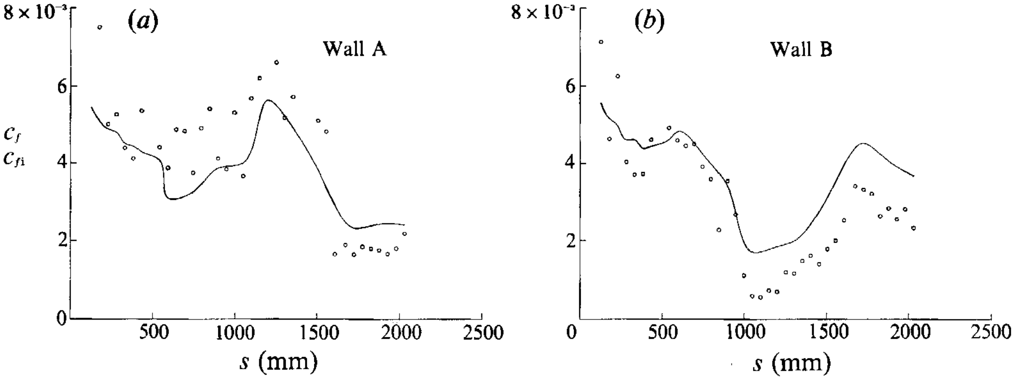

FIGURE 15. Skin friction c_{fi} calculated from internal-layer plots of mean velocity profiles (○) compared with conventional measurements of c_f (——).

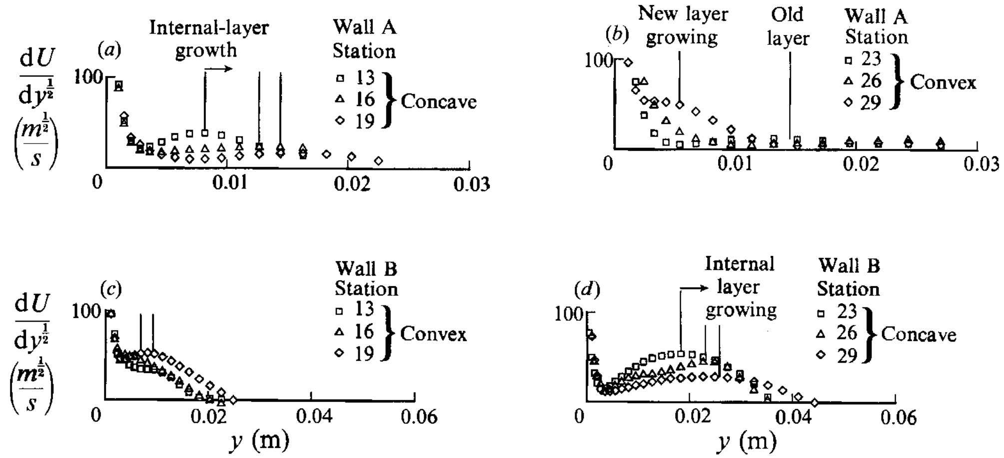

FIGURE 16. Curvature effects on outer-layer lengthscales.

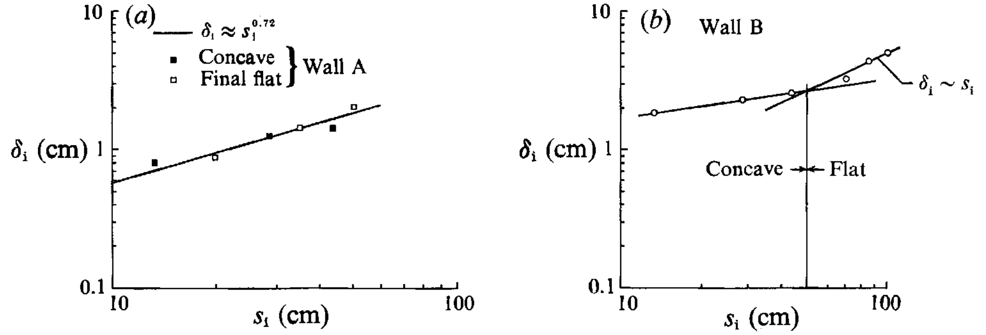

FIGURE 17. Longitudinal distribution of the curvature effect on the growth of outer-layer lengthscales.

The streamwise distributions of these outer-layer thicknesses are shown in figure 17. For wall A, the growth rate exponent is 0.72 in the concave and final flat regions although there is a convex stretch in between. The same growth rate is also found in the internal layer formed at a smooth-to-rough surface junction on a flat wall at zero

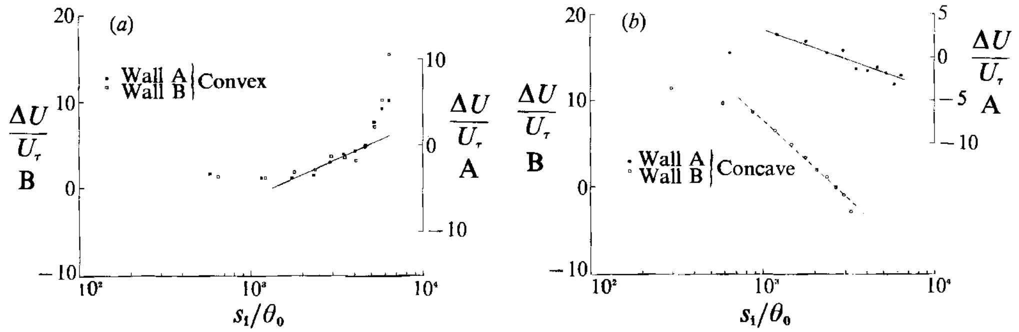

FIGURE 18. Longitudinal distributions of the strength of the wake component in the curved lengths. Lines: (a) asymptote in zero pressure gradient, (b) mean trends.

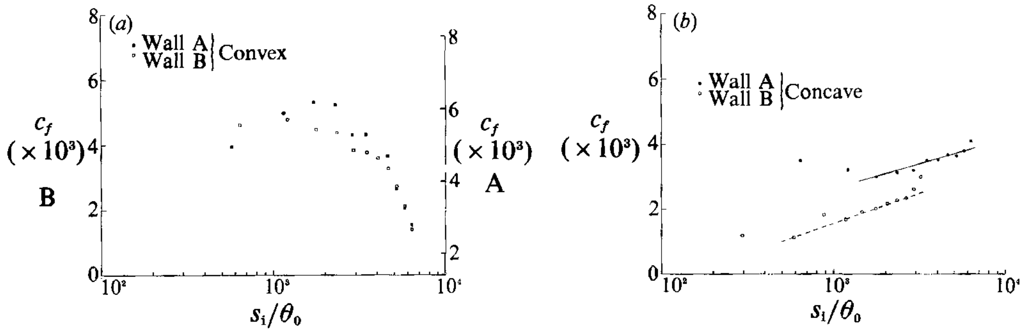

FIGURE 19. Skin friction development in internal-layer coordinates. Solid lines: mean trends.

pressure gradient (Bandyopadhyay 1987; Antonia & Luxton 1971). At wall B also, the growth rates have their origin at the curvature junctions although the exponent is lower and higher than 0.72 in the concave and final flat stretches, respectively.

7.3. *Wake component and skin-friction*

The streamwise distributions of the strength of the wake component, which is the maximum deviation from the law of the wall (figure 4), for the curved lengths are compared in figure 18. The wake component eventually increases and decreases in the convex and concave walls, respectively, as it is known to. For the two walls, the convex rates are identical but the concave rates are not. The convex distributions attain the asymptotic level for zero pressure gradient ($\Delta U^+ \sim 6.7 \log (s_i/\theta_0)$ known to be reached at $\delta/R > 0.05$ (Bandyopadhyay 1986). The rapid rise beyond the asymptote towards the end of the convex fetch occurs in a positive $\mathrm{d}p/\mathrm{d}s$ region which is known to have such an effect.

The skin friction distributions in each section are shown in figure 19 in internal-layer coordinates. The drop rates are identical for the convex walls. However, the rise rate is slightly higher for the concave fetch of wall B. In figure 19, the asymmetric response can best be seen by comparing the concave fetch in wall A with the convex fetch in wall B since they have a similar upstream flat plate. The characteristic curvature response for the concave length takes twice as long to appear. In figure 5, both concave walls show an s-delay of 100 to 200 mm before rising. The delay in the convex B wall is small (< 100 mm); the convex A wall has a larger delay (225 mm) before the characteristic drop but then it is preceded by a concave fetch. The

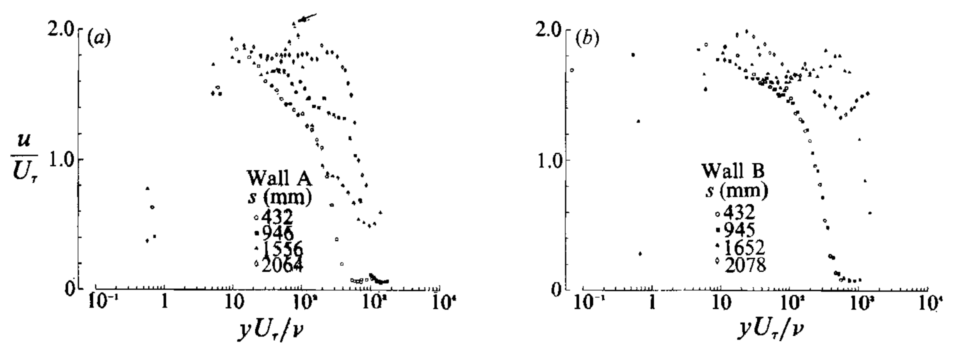

FIGURE 20. u-turbulence intensity profiles.

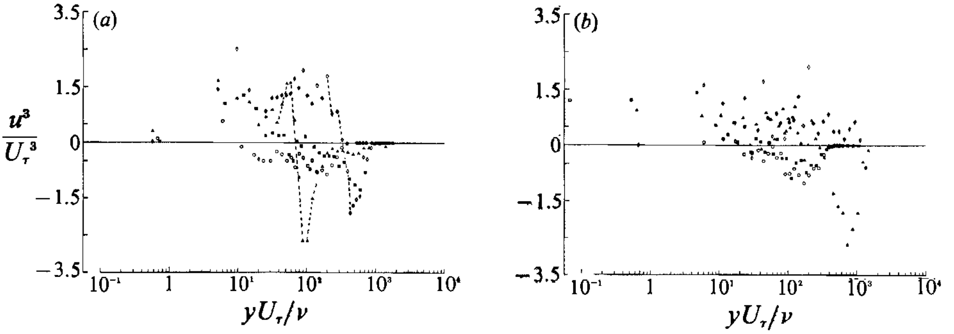

FIGURE 21. Profiles of longitudinal flux of the u-turbulence intensity. Symbols in (a, b) are as in figure 20(a, b), respectively.

response time of curvature has also been discussed by Barlow & Johnston (1988) and Muck *et al.* (1985).

8. Longitudinal turbulence intensity and diffusion

The profiles of u-turbulence intensity and its longitudinal flux were measured in the mid-plane at one station approximately toward the end of each section. The turbulence and its flux are shown in wall-layer coordinates in figures 20 and 21, respectively. To track the active turbulence longitudinally, the surface-normal distances are stretched by a factor, $f = \theta_f/\theta$, where θ_f and θ are momentum thicknesses at the final ($s = 2063.75$ mm for wall A and 2078.04 mm for B) and local stations, respectively. The intensity and flux are shown in figures 22 and 23, respectively, in the stretched coordinates. In the outer parts of both walls, the suppression of turbulence intensity due to convex curvature and the amplification due to concave curvature are marked in figure 22. The turbulence amplification takes place in the region where the mean velocity dips below the log law (figure 4). After the convex section in wall A, the intensity amplification at $fy^+ \sim 150$ (marked by arrow in figures 20*a* and 22*a*) and its broadening with downstream recovery ($s_i/\delta_0 = 0.96$ and 16.2, respectively in the final flat length) are present in the recovery measurements at $s_i/\delta_0 = 4$ and 17, respectively of Alving, Smits & Watmuff (1986, figure 10*a*) following a 90° convex turn. They called this a 'stress bore'. The wall B profile at the first recovery station after the concave fetch ($s = 1652$ mm) also contains a similar high stress region at $fy^+ \sim 50$. It is not clear if the bores originate at the final curvature-to-flat junctions.

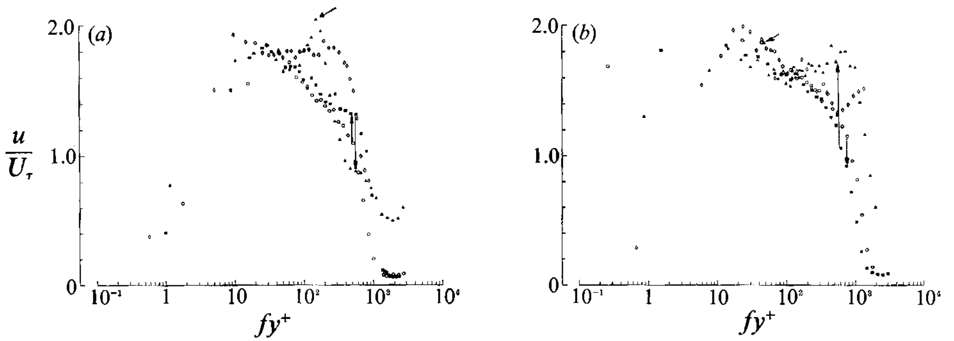

FIGURE 22. u-turbulence profiles in stretched y-coordinates. Symbols in (a, b) are as in figure 20(a, b), respectively.

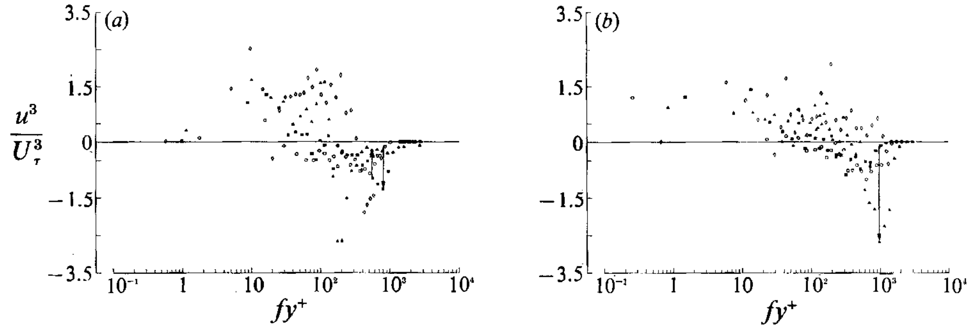

FIGURE 23. Profiles of longitudinal flux of the u-turbulence intensity in stretched y-coordinates. Symbols in (a, b) are as in figure 20(a, b), respectively.

In figure 23, the markings show that, in the outer region where the streamwise transport is associated with a deceleration, $|u^3/U_\tau^3|$ increases and decreases due to concave and convex curvatures, respectively. In the two recovery stations in figure 21(a), the data points are connected by a solid line in the region where the acceleration/deceleration carrying out the flux changes sign. The crossovers are very sharp compared to that in a typical flat-plate boundary layer ($s = 431.8$ mm, for example). They are located in the high stress region mentioned earlier.

9. Conclusions

Experiments have been carried out in two turbulent boundary layers subjected to abrupt changes in the external conditions such as curvature and pressure gradient. The flow geometry has its origin in the convex curvature concept of viscous drag reduction. In particular, the two curvature sequences and the curvature parameters have been chosen to determine the drag-reducing effects of the asymmetric response of turbulent boundary layers to concave and convex curvatures. The curvature parameters have been kept large.

The turbulent boundary layer on wall A, which is recovering from a sequence of concave-to-convex curvature, has a sustained lower skin friction in the final flat recovery section than that on wall B where the recovery is from a sequence of convex-to-concave curvature. The recovery on A is not complete at the last measurement station where $s_1/\theta_0 \approx 100$.

Taking the three-dimensional flow into account, the nett wall A friction drag is lower than that on the wall B by 12%.

The wall shear stress trend could be computed from the mean velocity profile within a thin internal boundary layer near the surface. However, τ_w values do not change exactly at the curvature junction. When the preceding section is flat, the delay is ≈ 150 mm in a concave wall but < 100 mm in the convex wall.

The spanwise non-uniformities in the concave regions agree with the Görtler stability diagrams if kinematic viscosity is replaced by turbulent eddy viscosity.

The corner vortices extend over most of the flow field on wall B unlike that on wall A. The growth of the corner vortex is accompanied by an increasing spanwise non-uniformity in the skin friction. The phase reverses in the corners.

The defect profiles show the existence of an interesting curvature-characteristic layer at a constant y/θ ($= 4.2$ to 4.5) which demarcates the downstream gradient of the vertical shear.

When the pressure gradient is large, the departure and return to equilibrium display an hysteresis-like effect on large eddies. The departure from equilibrium with increasing pressure gradient is linear in character but the return to equilibrium during the withdrawal of pressure gradient is nonlinear.

After perturbation, the outer-layer lengthscales show the following characteristic trends for each flat recovery and curved section. They grow in the concave and final flat recovery regions. For wall A, the growth rate is akin to that in internal layers due to a smooth-to-rough surface perturbation but, for wall B, it is not. However, the growth is suppressed (for wall A) or marginally changes (for wall B) in the convex walls.

In both convex regions, the strength of the wake component reaches the zero-pressure-gradient asymptotic limit. However, in the concave fetches, the streamwise drop is much faster for wall B.

In the outer layer, the amplification and suppression of u-turbulence intensity take place on the concave and convex walls, respectively. They are accompanied by decreased and increased streamwise flux, respectively. The flat-wall recovery for wall A displays a thin high stress region at $y^+ \sim 80$ where the flux also changes sign sharply. A similar near-wall high stress region is present in the recovery section of wall B also.

The support of NASA (P.R.B. NAS1-18458 and A.A. NAS1-18599) is gratefully acknowledged. The assistance of Messrs M. Javed and E. Varella is also acknowledged. Mr J. B. Anders is thanked – his interest made this work possible. The authors are also grateful to the referees for their suggestions.

REFERENCES

ALVING, A. E., SMITS, A. J. & WATMUFF, J. H. 1986 Turbulent boundary layer relaxation from convex curvature. *J. Fluid Mech.* **211**, 529–556.

ANTONIA, R. A. & LUXTON, R. E. 1971 The response of a turbulent boundary layer to a step change in surface roughness. Part 1. Smooth to rough. *J. Fluid Mech.* **48**, 721–761.

BANDYOPADHYAY, P. R. 1986 Review – Mean flow in turbulent boundary layers disturbed to alter skin friction. *Trans. ASME J. Fluids Engng* **108**, 127–140.

BANDYOPADHYAY, P. R. 1987 Rough-wall turbulent boundary layers in the transition regime. *J. Fluid Mech.* **180**, 231–266.

BANDYOPADHYAY, P. R. 1988 Resonant flow in small cavities submerged in a boundary layer. *Proc. R. Soc. Lond.* A **420**, 219–245.

BANDYOPADHYAY, P. R. 1989 Viscous drag reduction of a nose body. *AIAA J.* **27**, 274–282.

BANDYOPADHYAY, P. R. 1990 Convex curvature concept of viscous drag reduction. In *Viscous Drag Reduction in Boundary Layers* (ed. D. M. Bushnell & J. N. Hefner), vol. 123, pp. 285–324. AIAA.

BARLOW, R. S. & JOHNSTON, J. P. 1988 Structure of a turbulent boundary layer on a concave surface. *J. Fluid Mech.* **191**, 137–176.

BASKARAN, V., SMITS, A. J. & JOUBERT, P. N. 1987 A turbulent flow over a curved hill. Part 1. Growth of an internal layer. *J. Fluid Mech.* **182**, 47–83.

BRADSHAW, P. 1969 The analogy between streamline curvature and buoyancy in turbulent flow. *J. Fluid Mech.* **36**, 177–191.

BRADSHAW, P. 1973 Effects of streamline curvature on turbulent flow. *AGARD AG*-169.

BUSHNELL, D. M. 1983 Turbulent drag reduction for external flows. *AIAA Paper* 83-0227.

CLAUSER, F. H. 1956 The turbulent boundary layer. *Adv. Appl. Mech.* **4**, 1–51.

ERM, L. P., SMITS, A. J. & JOUBERT, P. N. 1985 Low Reynolds number turbulent boundary layers on a smooth flat surface in a zero pressure gradient. In *Fourth Symp. on Turbulent Shear Flows, Aug. 7–9, 1985, Cornell University*, pp. 2.13–2.18.

GATSKI, T. B. & SAVILL, A. M. 1989 An analysis of curvature effects for the control of wall-bounded shear flows. *AIAA Paper* 89-1014.

GILLIS, J. C. & JOHNSTON, J. P. 1983 Turbulent boundary-layer flow and structure on a convex wall and its redevelopment on a flat wall. *J. Fluid Mech.* **135**, 123–153.

KÁRMÁN, T. VON 1934 Some aspects of the turbulence problem. In *Proc. Fourth Intl. Congr. of App. Mech., Cambridge University*, p. 54.

KIM, S.-W. 1989 Numerical investigation of an internal layer in turbulent flow over a curved hill. *NASA TM* 102230.

LEONTEV, A. & FOMICHEV, V. M. 1983 Heat transfer and drag in a turbulent boundary layer with a pressure gradient. *Inz. Fiz. Zh.* (in Russian) **45**, 5–11.

MOSER, R. D. & MOIN, P. 1987 The effects of curvature in wall-bounded turbulent flows. *J. Fluid Mech.* **175**, 479–510.

MUCK, K. C., HOFFMANN, P. H. & BRADSHAW, P. 1985 The effect of convex surface curvature on turbulent boundary layers. *J. Fluid Mech.* **161**, 347–369.

NASH, J. F. 1965 Turbulent boundary-layer behavior of the auxiliary equation. *AGARDOgraph* 97, pp. 245–279.

NASH, J. F. & PATEL, V. C. 1972 *Three-Dimensional Turbulent Boundary Layers.* SBC Tech. Books, Sci. and Bus. Consultants, Inc., Atlanta, Ga.

PATEL, V. C. 1965 Calibration of the Preston tube and limitations on its use in adverse pressure gradients. *J. Fluid Mech.* **23**, 185–208.

PRABHU, A., NARASIMHA, R. & RAO, B. N. S. 1983 Structure and mean flow similarity in curved turbulent boundary layers. *Proc. IUTAM Symp. on Structure of Complex Turbulent Shear Flows, Marseille, 1982* (ed. R. Dumas & L. Fulachier). Springer.

PRANDTL, L. 1929 *Sonderdruk aus Vortrage aus dem Gebiete der Aerodynamik und Verwandter Gebiete.* Aachen. (Transl. *NACA TM* 625).

PURTELL, L. P., KLEBANOFF, P. S. & BUCKLEY, F. T. 1981 Turbulent boundary layer at low Reynolds numbers. *Phys. Fluids* **24**, 802–811.

RAMAPRIAN, B. R. & SHIVAPRASAD, B. G. 1977 Mean flow measurements in turbulent boundary layers along mildly curved surfaces. *AIAA J.* **15**, 189–196.

REHMAN, F. & BOWYER, J. M. 1989 Turbulent incompressible air flow through S-shaped ducts with cross-sectional area change. *Forum on Turbulent Flows.* ASME FED-76, pp. 49–57.

RICHMOND, M. C., CHEN, H. C. & PATEL, V. C. 1986 Equations of laminar and turbulent flows in general curvilinear coordinates. *IIHR Rep.* 300. Iowa Inst. of Hyd. Res.

SCHLICHTING, H. 1979 *Boundary-Layer Theory*, 7th edn. McGraw-Hill.

SCHMIDT, M. C., WHITELAW, J. H. & YIANNESKIS, M. 1987 Flow in out-of-plane double S-bends. In *6th Symp. on Turbulent Shear Flows, Toulouse, Sept. 7–9*, pp. 13.3.1–13.3.6.

SMITH, A. M. O. 1955 On the growth of Taylor–Görtler vortices along highly concave walls. *Q. Appl. Maths* **13**, 233–262.

Smits, A. J., Matheson, N. & Joubert, P. N. 1983 Low Reynolds number turbulent boundary layers in zero and favorable pressure gradients. *J. Ship Res.* **27**, 147–157.

Smits, A. J., Young, S. T. B. & Bradshaw, P. 1979 The effect of short regions of high surface curvature on turbulent boundary layers. *J. Fluid Mech.* **94**, 209–242.

So, R. M. C. 1975 A turbulence velocity scale for curved shear flows. *J. Fluid Mech.* **70**, 37–57.

So, R. M. C. & Mellor, G. L. 1972 An experimental investigation of turbulent boundary-layers along curved surfaces. *NASA CR*-1940.

So, R. M. C. & Mellor, G. L. 1973 Experiment on convex curvature effects in turbulent boundary layers. *J. Fluid Mech.* **60**, 43–62.

So, R. M. C. & Mellor, G. L. 1975 Experiment on turbulent boundary layers on a concave wall. *Aero. Q.* **26**, 25–40.

Spalart, P. R. 1988 Direct numerical simulation of a turbulent boundary layer up to $Re_\theta = 1410$. *J. Fluid Mech.* **187**, 61–98.

Tani, I. 1962 Production of longitudinal vortices in the boundary layer along a concave wall. *J. Geophys. Res.* **67**, 3075–3081.

Townsend, A. A. 1976 *The Structure of Turbulent Shear Flow.* Cambridge University Press.

Tsai, H. M. & Leslie, D. C. 1990 Large eddy simulation of a developing turbulent boundary layer at low Reynolds number. *Intl J. Num. Meth. Fluids* **10**, 519–555.